Powder Technology 485 (2027) 123155

Contents lists available at ScienceDirect

Powder Technology

journal homepage: www.journals.elsevier.com/powder-technology

Scalable dry processing of solid-state battery cathode composites via high-intensity mixing and assisted fluidized beds

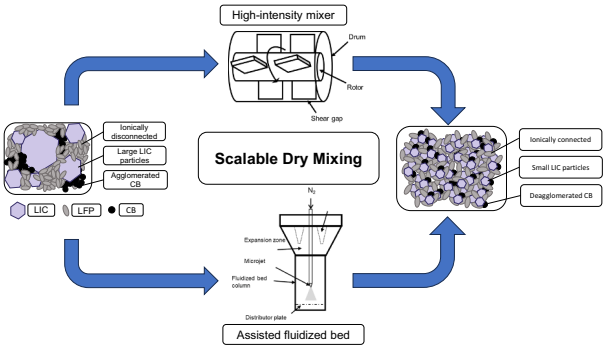
Zhi Cheng Hua [a,*,1], Finn Frankenberg [b,1], Maximilian Kissel [c], Jürgen Janek [c], Stefan Heinrich [a], Arno Kwade [b]

[a] Institute of Solids Process Engineering and Particle Technology, Hamburg University of Technology, Germany
[b] Institute for Particle Technology, Technical University of Braunschweig, Germany
[c] Institute of Physical Chemistry & Centre for Material Research, Justus-Liebig-University Gießen, Germany

HIGHLIGHTS

- Scalable dry mixing of solid-state battery (SSB) cathodes was successfully demonstrated using a vibration jet-assisted fluidized bed and a high-intensity mixer.
- Both processes achieved comparable microstructures and terminal discharge capacities of approximately 110mAh/g.
- The discharge capacity is primarily governed by the comminution of the solid electrolyte (Li_3InCl_6) and the resulting homogeneity of the ionic percolation network.
- The assisted fluidized bed proved to be significantly more energy-efficient, requiring 4 to 6 times less specific energy input than the high-intensity mixer for a comparable microstructure.
- Electronic powder conductivity was identified as a reliable, rapid proxy for evaluating microstructural quality and predicting achievable discharge capacity.

GRAPHICAL ABSTRACT



ARTICLE INFO

Keywords:
Solid-state batteries
Dry processing
Scalable mixing
Assisted fluidized bed
Highintensity mixing
Cathode composites

ABSTRACT

This study investigates the scalable mixing capability of a vibration jet-assisted fluidized bed as well as a high-intensity mixer for the dry mixing of cathode composites for solid-state battery (SSB) cathodes. Despite having different working principles, both processes yield comparable microstructural and thus electrochemical results, proving their applicability for SSB manufacturing. Correlating structural analysis via SEM image analysis with electrochemical data reveals that the discharge capacity is mainly governed by the comminution of the solid electrolyte Li_3InCl_6 (LIC) and the homogeneity of the microstructure which ultimately determines the hetero-contact number between active material and the ionic and electronic network. For both processes the stress

* Corresponding author.
E-mail address: zhi.cheng.hua@tuhh.de (Z.C. Hua).
[1] These authors contributed equally.

https://doi.org/10.1016/j.powtec.2026.123155
Received 22 April 2026; Received in revised form 7 August 2026; Accepted 26 August 2026
Available online 28 August 2026
0032-5910/© 2026 The Authors. Published by Elsevier B.V. This is an open access article under the CC BY license (http://creativecommons.org/licenses/by/4.0/).

intensity is identified as the main cause for comminution of LIC and deagglomeration of the active material $LiFePO_4$ (LFP) and conductive additive carbon black (CB). An inverse relationship between electronic and ionic percolation is found: the mixing process disrupts long range electronic percolation due to CB deagglomeration and LIC comminution, whereas the smaller solid electrolyte particle size significantly increases the ionic percolation and therefore cell capacity. Overall, this study proves that both processes are promising for an up-scaled dry mixing process of SSB cathode materials.

1. Introduction

Solid-state batteries (SSBs) have emerged as a promising further development of conventional lithium-ion batteries (LIBs), as they are expected to enable the use of a lithium metal anode and thereby higher energy densities [1–3]. However, SSBs face various manufacturing challenges regarding improper cathode microstructure [4], high production cost and environmental issues when wet processed with toxic, organic solvents [5–7].

Dry processing could circumvent these side reactions by avoiding the use of a solvent, and also the need for solvent drying and recovery steps, which additionally improves the energy efficiency of production [2,8–10]. However, dry processing faces several challenges such as agglomeration of fine particles [11–13], poor mixture [14,15], or large solid electrolyte particles [16], which hinder sufficient electronic and ionic percolation in the cathode. Those microstructural challenges can also result in high interfacial resistances between particle contacts or poor percolation networks, thus impairing cell performance [5–7,15,17]. To optimize the cathode microstructure for high-performance cells, a homogeneous distribution of components, continuous ionic and electronic pathways, and mechanically robust particle-particle contacts are essential [12,15,18,19]. In particular, these particle-particle contacts are important at heterogeneous interfaces (heterocontacts), i.e., between dissimilar particle species such as active material and solid electrolyte as well as and conductive additives as they determine the charge transfer kinetics.

The microstructure of a SSB mixture mainly arises from the applied processing method [20], which is why a precise control of processing conditions is essential. In contrast to LIBs in which a liquid electrolyte fills up the electrodes' pores and provides sufficient ionic percolation [21], in SSBs the effective ionic conductivity in the cathode is based solely on solid-solid contacts [22]. To increase the number of mechanical contacts, a reduction in solid electrolyte particle size due to deagglomeration or comminution, adapted to the particle size distribution of the active material and proper mixing becomes crucial [23,24]. Previous studies have corroborated the relevance of dry mixing methods in SSB cathode mixtures [14,25–27]. These show that the mixing process significantly impacts the cathode microstructure due to deagglomeration of large solid electrolyte particles and proper mixing of the materials [25,26]. However, challenges like agglomeration or poor mixing can result in an insufficient and inhomogeneous microstructure thus leading to strongly deviating electrochemical performances. The relevance of solid electrolyte particle size and its spatial distribution for the solid/solid interface and overall cell performance has previously been demonstrated for sulfide-based systems [28] albeit using lab-scale comminution and cell-level design approaches. Our work complements these findings by addressing the scalable, solvent-free generation of such favorable microstructures.

Especially when particles become smaller, interparticle forces like van der Waals or electrostatic forces dominate over gravitational forces [11], which results in strong agglomeration, thus preventing a high number of heterocontacts [25,29–31]. Therefore, the purpose of up-scaled mixing processes with cohesive particles is to continuously break the particles, either of the same materials or of different materials, to finally achieve a homogenous microstructure [32,33]. Recent advances in high-intensity mixing and fluidized bed processing offer potential solutions in overcoming microstructural shortcomings, enabling effective agglomerate dispersion and thus powder homogeneity without the use of solvents [25,26]. Here, the mechanical stress applied to the powder mixture seems to play a major role in electrolyte break down and thus optimization of SSB cathode microstructure [18,24–26,34–36]. Especially, collision energy of particles or grinding media with particle beds, often referred to as stressing energy, is the crucial factor determining the deagglomeration and thus also cathode composite formation [37–40].

Current mixing methods are often conducted on lab scale with mortar and pestle or small frequency or planetary ball mills [14,27]. Attempts to up-scale the milling processes show promising results [25,26]. However, the fundamental mechanisms governing deagglomeration and microstructure formation remain largely unexplored for larger-scale mixing devices. Additionally, the manual processing of the solid electrolyte by a mortar and pestle often results in different microstructures and electrochemical performance, as the applied stress is not controlled.

This study investigates and compares high-intensity mixing with vibration and jet assisted fluidized bed processing for the scalable dry mixing of SSB cathode materials, evaluating their electrochemical performance, microstructure and stressing conditions. We first analyze particle dynamics in both processes, followed by an examination of stress-induced deagglomeration and microstructure formation. To investigate both processes, a model SSB system including $LiFePO_4$ (LFP) as active material, in-house synthesized Li_3InCl_6 (LIC, see Fig. S5 and S6 in SI for ionic conductivity and X-ray diffractogram) as solid electrolyte and carbon black (CB) as conductive additive is applied. LFP and LIC are selected for their moisture stability and non-toxic nature, while nano-scale CB shall ensure percolating electronic pathways. A special aspect of this material combination is that both the active material ($x_{50,3} = 0.5\ \mu m$) and the conductive additive ($x_{50,3} \sim 40$ nm) consist of primary particles much smaller than 1 μm and are therefore highly cohesive in nature. Small active material particles may be favorable due to their fast charge transport kinetics [19]. In contrast, the solid electrolyte (LIC) exhibits a broad particle size distribution, ranging from primary particles of approximately 100 nm to large aggregated clusters measuring several tens of micrometers, thus making comminution of LIC essential besides the actual mixing of the three components.

While this study utilizes LIC and LFP as a model system due to their ambient stability, the translation of these dry processing techniques to industrially relevant materials (e.g., NMC active materials, sulfide- or oxide-based solid electrolytes) requires careful consideration of their intrinsic mechanical properties. The comminution and deagglomeration behavior in high-intensity mixers and assisted fluidized beds is fundamentally governed by the materials' fracture toughness and Young's modulus. For instance, sulfide solid electrolytes generally exhibit high ductility and lower Young's moduli compared to the significantly harder and more brittle oxide-based materials [41–44]. In comparison, the mechanical properties of halide SE's like Youngs modulus have only been theorized in a single study and are therefore not known [45]. Consequently, the required stress intensities for effective processing will vary substantially depending on the target material system.

2. Experimental setup and materials

2.1. SSB materials

In this study LFP (Johnson Matthey Battery Materials GmbH, Germany), CB (C-NERGY SUPER C65, IMERYS) and LIC were used to create cathode mixtures with a mass ratio of 58:4:38. LIC was in-house synthesized via water-mediated synthesis (see [26,46]), and after synthesis comminuted for 4 min at 600 rpm with a milling bead size of 5 mm in a planetary ball mill (Pulverisette 7, Fritsch GmbH).

2.2. Assisted fluidized bed

An assisted fluidized bed system was employed to mix the SSB powders and to overcome the cohesive forces between the sub-micron sized particles. This setup expands on the design by Hua et al. [25], scaling the fluidized bed diameter from previously 5 cm to 10 cm to accommodate larger batch processing, as well as preventing elutriation due to lower superficial gas velocities. The system utilizes a piston-crank mechanism to generate vertical vibration. The vibration frequency was set to 17.6 Hz with an amplitude of 1 mm.

Dry nitrogen (Grade 5.0) served as the fluidization gas, with its flow rate regulated to 15 L/min by a mass flow controller (El-Flow Select, Bronkhorst GmbH, Germany). This flow rate corresponds to a superficial gas velocity of 3.18 cm/s, optimized to balance particle elutriation and bed fluidization. The expansion zone integrates two filtration stages: primary filtration via 5 μm porous metal filter candles (GKN Sinter Metals GmbH, Germany) and secondary filtration through a HEPA 13 filter to ensure particle retention. To maintain consistent operation, an air-pressure-driven vibrator (Netter GmbH, Germany) was installed on the expansion chamber walls to periodically dislodge accumulated particles from the filter surfaces.

Deagglomeration was further enhanced through jet assistance. Dry nitrogen at 7 bar was delivered through height adjustable nozzles with orifice diameters of 0.4 mm and 0.8 mm, reaching a velocity of 320 m/s at the choke point [25]. The nozzle positioning can be dynamically altered via a lancet height adjustment mechanism. In this study, the nozzle height was set to 1 cm or 10 cm. A schematic of the full system, including the integrated vibration and jet assistance components, is provided in Fig. 1a.

Mixing of LFP, LIC and CB was performed for up to 90 min with a batch size of 100 g in total. An overview of the parameters can be found in Table 1.

As shown by Hua et al. the fluidization of cohesive battery powders requires sufficient stressing, e.g. by the implementation of the high velocity gas jet, which promotes deagglomeration and improves homogeneous mixing [25]. In general, there are different stressing mechanisms considered related to jets that act upon particles and agglomerates that lead to comminution and deagglomeration (Fig. 1b). First, upon entering the gas jets' flow field particles experience shear forces due to velocity gradients, which ultimately result in drag forces. Secondly, particles may experience collisional forces both with other particles as well as with walls. Third, when the jet injects gas flows with high velocities, vortices form that enhance shear forces and mixing further.

2.3. High-intensity mixing

A high intensity mixer (Picoline with Nobilta attachment, Hosokawa Alpine AG, Germany) was used to mix the same powders (LFP, LIC, CB)

Table 1
Overview of LFP-LIC-CB mixing with the vibration assisted fluidized bed.

	V1	V2	V3
Nozzle height [cm]	1 cm	1 cm	10 cm
Orifice diameter [cm]	0.4 mm	0.8 mm	0.8 mm

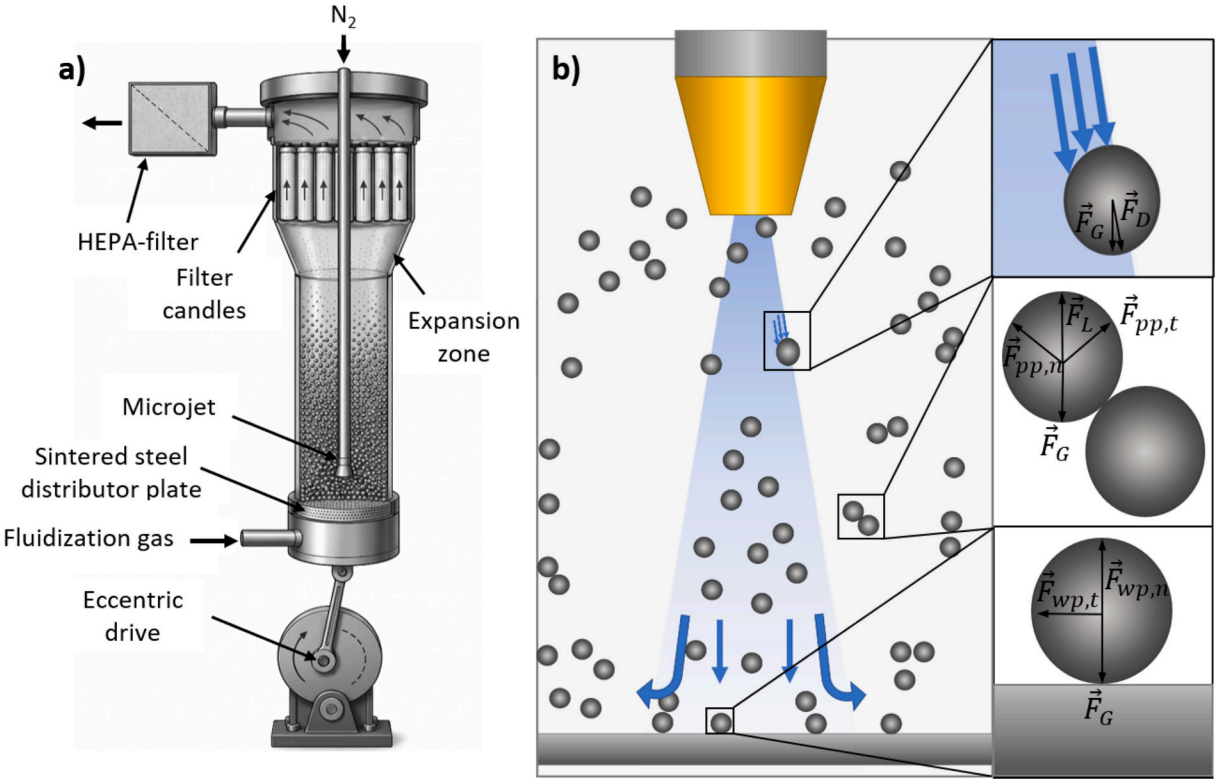


Fig. 1. a) Schematic drawing of the assisted fluidized bed with high velocity jet assistance. b) Overview on the forces acting on the particles in the assisted fluidized bed.

as with the assisted fluidized bed (Fig. 2a). Each batch consisted of 15 g and was mixed up to a tip speed v_{tip} of up to 40 m/s with a total mixing time of $t = 60$ min each. In this type of mixer, three main types of stressing mechanisms act upon particles that can lead to mixing, comminution and deagglomeration of particles: stressing in the gap between the rotor and the wall, particle-particle collisions and particle-wall collisions at the rotor blade (Fig. 2b) [26]. Frankenberg et al. found that the lowest stressing intensities are found outside the gap followed by the stressing intensity within the gap that occur due to the compression and shearing of the particles [26]. The highest stressing intensity is found at the rotor blade that is caused by the collision of particles with the rotor blade, making the tip speed of the rotor and the relative velocity to the particles the primary cause for comminution and deagglomeration.

2.4. Electrochemical characterization methods

2.4.1. Electronic powder conductivity

Electronic powder conductivity was measured using a Zwick 020 material tester (ZwickRoell GmbH & Co. KG, Germany) placed within a dry room, in combination with a Digistant® 4420 universal calibrator (Burster GmbH & Co. KG, Germany). Three samples of 1 g each of the SSB cathode powder mixture were compressed in a measurement cylinder. Constant currents of up to 10 mA were applied using the calibrator dependent on the measured voltage until a compaction pressure of 3.45 MPa was reached. The voltage across the powder bed was continuously monitored, and the specific conductivity σ_{spec} at 3.45 MPa was calculated using the resistance derived from Ohm's Law, the powder bed height l, and its cross-sectional area A (Eq. (1)).

$$\sigma_{spec} = \frac{l}{R \bullet A} \tag{1}$$

2.4.2. Solid-state battery cell assembly

SSB half-cell assembly was carried out in an argon-filled glove box with impurity levels of $p(O_2)/p < 1\ ppm$ and $p(H_2O)/p < 1\ ppm$. First, the separator was built by filling 40 mg of Li_6PS_5Cl (LPSCL, NEI corp., USA) in a cell chamber with a diameter of 10 mm and pressed with hand pressure. A second separator layer towards the cathode side was built with 40 mg in-house synthesized LIC and again pressed by hand. Then, approximately 11 mg of the produced SSB cathode mixture was evenly distributed on the LIC layer. The whole cell was then uniaxially compacted at 380 MPa for 3 min. An In/(InLi) alloy anode is fabricated using 9 mm diameter indium foil (100 µm thickness, 99.9999%, ChemPUR, Germany) along with a 6 mm in diameter lithium foil (100 µm thickness, China Energy Lithium, China) and placed on top of the LPSCL layer.

For electrochemical testing, the cell was fixed in a steel frame with 4 symmetrical screws and threaded rods and tightened with 10 Nm of torque corresponding to a nominal stack pressure of approximately 80 MPa. The cells rested for 6 h to enable the diffusion of indium and lithium. The built cells were then cycled at 0.1C between 1.9 V and 3.4 V vs In/InLi.

2.5. SEM image analysis for microstructural investigation

SEM images were acquired of compacted pellets of the SSB mixtures (Phenom XL, Life Technologies GmbH, Germany). The pellets were pressed using a laboratory press (LaboPress P200S, Vogt Labormaschinen, Germany) in which the powder was compacted at 380 MPa for 3 min to mimic the compaction pressure that is also applied for the cell building. A backscatter detector is used to differentiate between the particle phases which result in LIC appearing as white/light-grey, LFP being detected as dark-grey and carbon black (as well as pores) appearing as black.

The SEM images of the compacted pellets were analyzed to determine the distribution and particle size of LIC within the composite. Images acquired at 2000× magnification were processed and segmented using the *Trainable Weka Segmentation* plugin in Fiji. Three primary classes were defined based on grayscale contrast: LIC (bright regions), LFP (grey regions), and a combined class containing carbon black (CB) and pores (both appearing dark). Subsequent analysis focused on the segmented LIC phase. An in-house Python script was used to remove isolated single-pixel artifacts to reduce noise, and to compute the area-equivalent particle diameter d from the segmented regions (Eq. (2)).

$$d = 2 \cdot \sqrt{\frac{A}{\pi}} \tag{2}$$

The calculated equivalent diameters were then used to derive number-based q_0 particle size distributions as well as volume-weighted q_3 particle size distributions. Conversion from q_0 to q_3 was performed by

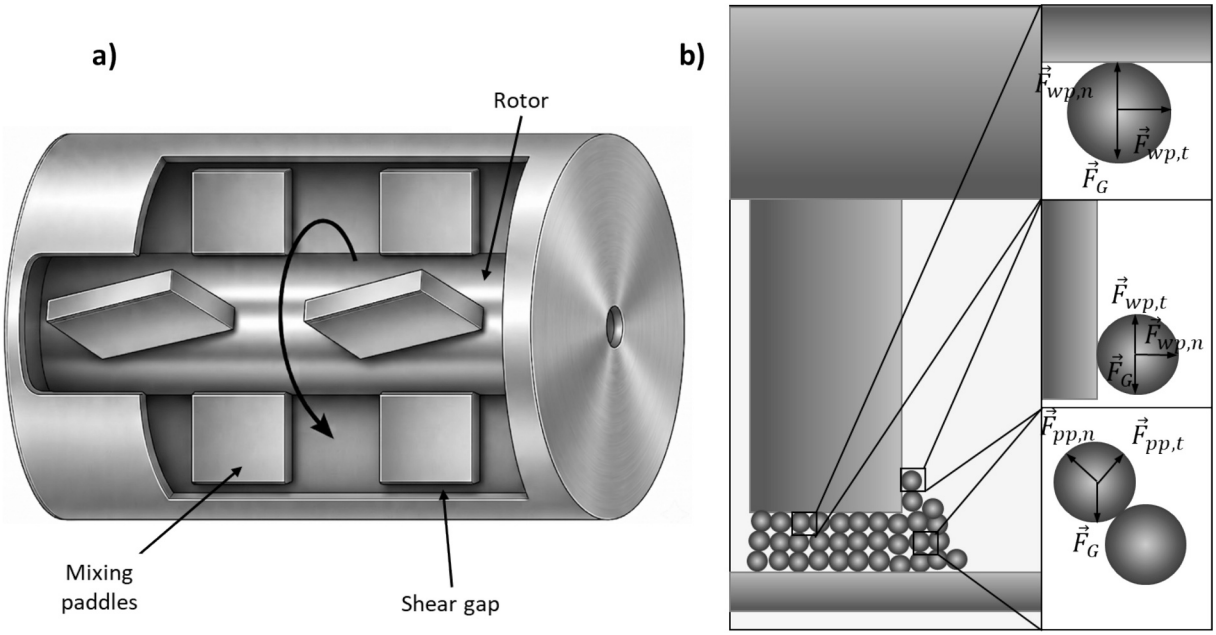


Fig. 2. a) Schematic of the high intensity mixer. b) Stressing conditions and forces acting on the particles within the high intensity mixer.

weighting each equivalent diameter with its proportional particle volume d^3, summing these weights within each size bin k, and finally normalizing by dividing the weight of each bin by the total weight across all bins and particles N (Eq. (3)).

$$q_{3,k} = \frac{n_k \bullet d_k^3}{\sum_{i=1}^{N} n_i \bullet d_i^3} \quad (3)$$

3. Results and discussion

3.1. Particle size of LIC

One major task of the mixing process is to distribute all three components (LIC, LFP, CB) in such a way that the number of heterocontacts between the three species is increased, thereby increasing the achievable discharge capacity of the SSB mix. Besides mixing, also the comminution of LIC (Fig. 3a) was found to be of utmost importance in our previous studies [25,26]. Here, a broad particle size range becomes visible containing small particles of about less than 1 μm up to 50 μm sized particles. This broad particle size range with large chunks of agglomerated and aggregated LIC is also visible from the SEM images (Fig. 3b).

With low intensity mixing, these chunks are not sufficiently well comminuted thus leading to a low number of heterocontacts between LIC-LFP-CB [25,26]. This results in low discharge capacities, which is why it is essential to break down the LIC particles and to ensure more contacts to be formed.

3.2. Microstructural image analysis of LIC-LFP-CB mixtures

The microstructural analysis of the pelletized samples of cathode powders processed in the assisted fluidized bed for 1 min and 60 min (Fig. 4a,b) show the progression of the mixing process and its effect on the materials microstructure. It becomes visible that from 1 min to 60 min of mixing a strong decrease in LIC particle size takes place thus leading to a much more homogeneous microstructure. The same observation can be made for the high-intensity mixer in which an increase in the tip speed from 4 m/s to 40 m/s leads to a significant LIC size decrease (Fig. 4c,d). A comparison of the SEM images from both the assisted fluidized bed and the high-intensity mixer (40 m/s) after 60 min of mixing shows a qualitatively comparable microstructure.

To further analyze the SEM images, the in-house python tool was applied to calculate particle sizes of LIC, based on segmented SEM images (Fig. 5a). Here the q_3 particle size distribution is used to quantify the main PSD descriptors like x_{10}, x_{50} and x_{90} from the pelletized powder. It should be noted that, while this procedure is highly time-efficient, it is also limited by the resolution of the SEM images, which may not capture the finest LIC particles and by the limited number of measured particles. Consequently, minor deviations can occur during segmentation. Nevertheless, the method reliably reflects the overall trend, particularly with respect to the larger LIC chunks.

In Fig. 5b the particle size of LIC from assisted fluidized bed mixing is shown as a function of the mixing time. It is observed that the median particle size d_{50} decreases with an increase in mixing time from 10 μm to 2.5 μm. Additionally, the PSD gets narrower which is visible from the decrease in the x_{90} which strongly decreases from 25 μm to about 5 to 7.5 μm. Both reductions mean that during the mixing process the LIC particles are comminuted. In turn this reveals that the applied stress intensity due to the nitrogen jet is sufficient to comminute large LIC particles and that here the stress number due to an increase in mixing time is essential to further breakup the LIC particles during the process. An increase in x_{90} between 60 min and 90 min of processing time in the assisted fluidized bed is likely attributed to the limited number of particles that were analyzed using SEM.

For the high-intensity mixer, the particle size of the LIC strongly decreases with an increase in tip speed at constant mixing time of 60 min (Fig. 5c). Here the x_{50} decreases from around 12 μm at a tip speed of 4 m/s to also about 2.5 μm at tip speeds of 40 m/s. This decreasing trend in the median particle size is also reflected in the x_{90}, which decreases from roughly 20 μm to about 7.5 μm with increasing tip speed. As all samples have been mixed for 60 min, this means that here the stress intensity is the governing factor that determines the LIC comminution. This was already anticipated in our previous study [26] and is now corroborated by the PSD analysis. An increase in mixing time and thus stress number would probably not help to further comminute the LIC particles as the acting stress is insufficient to break up the LIC particles further after 30 min of mixing [26]. A further decrease of in particle size is thus only possible with even higher tip speeds similar to pin impact mills or eventually smaller gaps to the chamber wall.

One further effect of the mixing in both devices becomes apparent, which is the deagglomeration of CB clusters. Here a strong reduction of CB clusters is visible which, in addition to the LIC comminution, will affect the electronic powder conductivity of the SSB mix.

For both processes the comminution of LIC shows a lower limit for the x_{10} particle size of about 2 μm. This observation allows two plausible explanations: For one, the acquired SEM images and their segmented counterpart do not show any particles below the lower threshold that could influence the particle size distribution due to SEM resolution related issues. This means that in reality there are also finer particles present but these cannot be detected with the SEM and subsequent segmentation method. A second mechanistic explanation is that smaller particles are naturally more robust towards external forces and cannot be comminuted any further with the used processes. This is because the stress intensity is independent of particle size and only a function of collision speed for stressing by impacts, while the strength of particles increases with decreasing particle size [47,48].

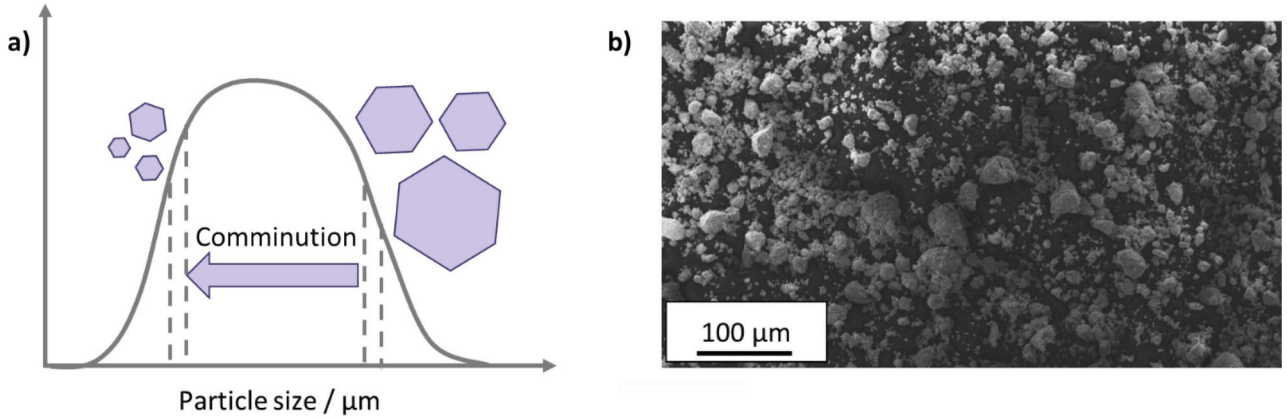


Fig. 3. a) Schematic particle size distribution of LIC. b) SEM-Image of in-house synthesized LIC after the comminution step but before mixing with LFP and CB.

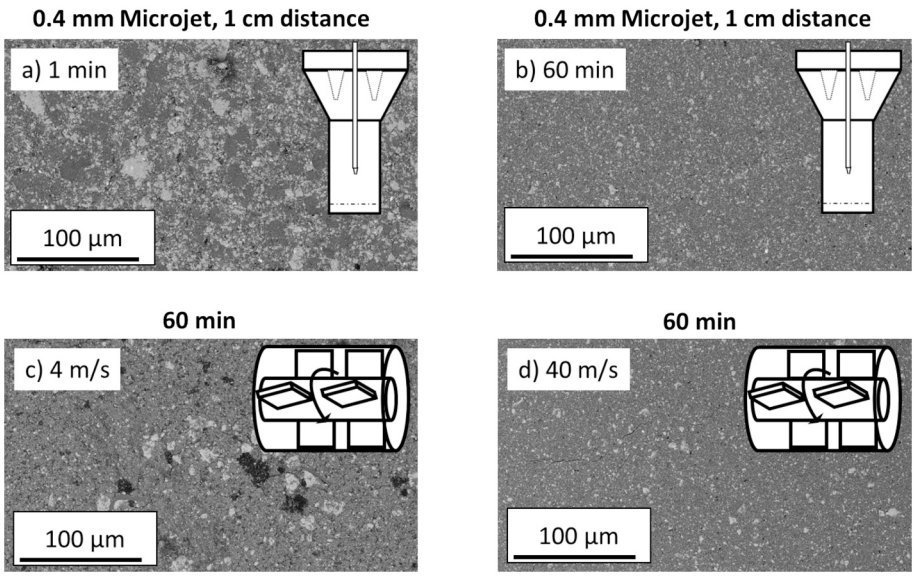


Fig. 4. SEM images of assisted fluidized bed mixing with a nozzle diameter of 0.4 mm, a distance of the nozzle to the distributor plate of 1 cm and a) 1 min processing time and b) 60 min processing time. SEM images of the mixtures from high-intensity mixing for 60 min at c) 4 m/s tip speed and d) 40 m/s tip speed.

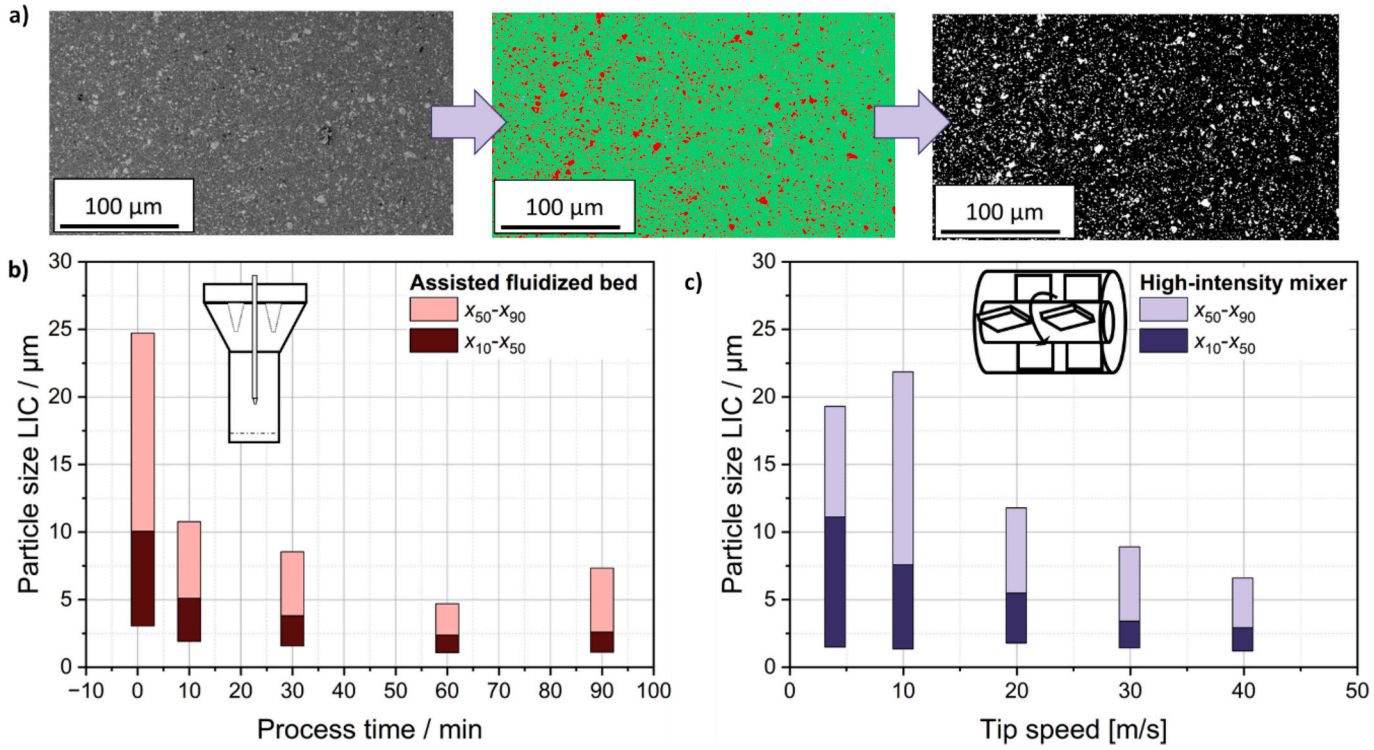


Fig. 5. a) SEM image segmentation workflow. LIC particle sizes obtained from image segmentation for b) of assisted fluidized bed mixing with a nozzle diameter of 0.4 mm and a distance of the nozzle to the distributor plate of 1 cm and different mixing times and c) high-intensity mixing for 60 min at different tip speeds.

3.3. Electronic powder conductivity as microstructural Indicator

Overall, both processes are capable of mixing submicron SSB particles and comminute LIC to improve the SSB microstructure. These microstructural changes strongly influence the electronic and ionic percolation within the cathode. First, this is reflected by the electronic powder conductivity which was measured for the SSB cathode mix at a compaction pressure of 3.45 MPa.

For the three assisted fluidized bed mixing variations related to nozzle diameter and distance to the distributor plate, a decrease in the electronic powder conductivity with increasing process time can be observed (Fig. 6a). This can be explained by two effects: The comminution of electronically insulating LIC particles which hinder electron transport and on the other hand the strong deagglomeration of CB clusters further amplifying this trend. In each case, the electronic powder conductivity shows a terminal electronic conductivity after about 60 min of mixing after which little change can be observed with further process time. This terminal electronic conductivity is lowest for the small nozzle diameter of 0.4 mm and a distance to the distributor plate of 1 cm (σ_{el} = at 60 min) and largest for the 0.8 mm nozzle diameter with

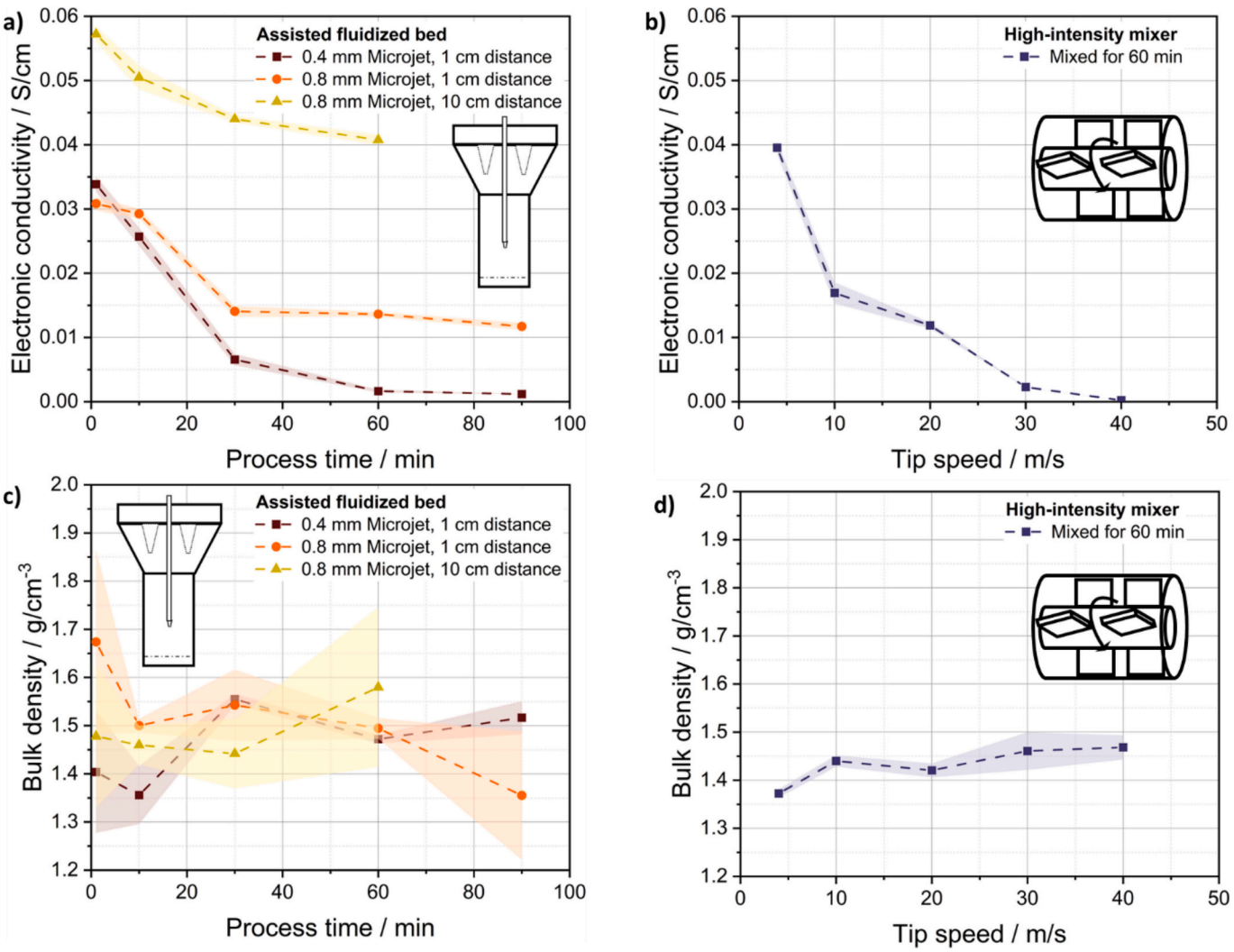


Fig. 6. a) Temporal evolution of electronic powder conductivity for the assisted fluidized bed mixtures at different nozzle diameters and nozzle distances. Measurements were conducted in triplicate. b) Electronic powder conductivity of the SSB mixtures prepared via high-intensity mixing at different tip speeds. c) Temporal evolution of the powder bulk density for the assisted fluidized bed mixtures at different nozzle diameters and nozzle distances. d) Powder bulk density of the SSB mixtures prepared via high-intensity mixing at different tip speeds.

a distance of 10 cm to the distributor plate (σ_{el} = at 60 min). These strong differences in the electronic conductivity reflect severe differences in the microstructure of the SSB mainly based on different LIC comminution and CB dispersion. The low electronic conductivity for the 0.4 mm nozzle diameter indicates a strong comminution of LIC particles and in parallel strong CB dispersion, thus resulting in enhanced insulation of the mixture. This enhanced comminution mainly stems from the lower distance to the distributor plate of only 1 cm compared to 10 cm, thus resulting in higher stress intensities acting on the particles. On the other hand, the larger distance between nozzle and distributor plate leads to lower stress acting on the particles due to lower collision velocities as particles decelerate on their way to the distributor plate. This lower stress intensity results in decreased comminution of LIC particles and is reflected in the higher electronic powder conductivity.

Comparing the mixing in the assisted fluidized bed with two different nozzle sizes (0.4 mm & 0.8 mm) but the same nozzle distance of 1 cm reveals a higher electronic powder conductivity for the larger nozzle diameter. In turn, this means that less comminution of LIC and dispersion of CB took place for the 0.8 mm nozzle and thus a lower stress intensity was acting on the particles. This is counter-intuitive at first, as doubling the nozzle diameter increases the volume flow four-fold which also increases the superficial gas velocity, since the fluidization gas flow was kept constant to prevent dead zones. As orifices become larger compared to the particles' inertia, the jet promotes advection of the particles along the jet streamlines because stokes number is very small for fine particles. This means, that particles that are very small will always advect while larger particles will detach from the flow. In this case they collide with the wall if they can be accelerated sufficiently by the jet and carry enough inertia. When increasing the nozzle size (0.8 mm compared to 0.4 mm), the streamlines caused by the jet also broaden causing the collision velocity of particles to drop due to deceleration near the distributor plate. Thus, the collision velocity and thus the stress intensity is lower for larger nozzles. We consider shear stressing and particle-particle collisions to be secondary mechanisms compared to particle-wall collisions in this setup. While literature confirms that particle-particle impacts primarily occur at the jet boundary where static bed material is entrained into the high-velocity stream, our data contradicts this being the dominant comminution factor.

In the high-intensity mixer the electronic powder conductivity decreases with an increase in tip speed for the SSB cathode mixtures which were all mixed for 60 min (Fig. 6b). In turn, this means that the higher the tip speed, the higher the stress intensity and thus the stronger the comminution of LIC and deagglomeration of CB. This mainly stems from the impact collisions of the particles with the fast rotating rotor as well

as the high shear stress within the gap of the mixing device [26]. However, when tip speed is increased, also the stress or collision number is increased, which means that for the same mixing time not only stresses are higher at increased tip speed but also the number of collisions that occurred during that time. However, it was shown previously [26] that after mixing for 30 min in the high-intensity mixer with 40 m/s tip speed, no significant further changes occur in the electrochemical performance (and thus microstructure) meaning that stress number is not the limiting factor but stress intensity.

Directly comparing the measured electronic powder conductivity of the high-intensity mixer with the assisted fluidized bed it becomes evident that the tip speed dependent trend is comparable to the time-dependent trend of the assisted fluidized bed for the small nozzle diameter (0.4 mm) and short distance to the distributor plate (1 cm). In turn this means, that comparable microstructures with comparable LIC comminution and CB deagglomeration were obtained.

The microstructural changes (LIC comminution, CB deagglomeration) are typically reflected in changing bulk densities as particles are differently packed [37]. Here, the bulk density was measured in the slightly compacted state (3.45 MPa) during the electronic powder conductivity measurement. For the assisted fluidized bed an increase in the bulk density with increasing mixing time can be observed for the mixture for which the 0.4 mm nozzle diameter was applied (Fig. 6c). This trend reflects the ongoing comminution of large LIC particles as well as deagglomeration of highly porous CB agglomerates. On the other hand, there is no clear trend of the bulk density evolution for the larger nozzle diameter and larger distance to the distributor plate. Continuous reagglomeration occured in these mixing experiments as well as an insufficient comminution of LIC and deagglomeration of CB which was already seen in the electronic powder conductivity evolution and particle size distribution (see Fig. 4 and Fig. 5).

The bulk density that was measured for the SSB mixtures prepared with the high-intensity mixer show an increase with increasing tip speed and thus stress intensity (Fig. 6d). This aligns well with the decreasing electronic powder conductivity, as LIC is comminuted and CB deagglomerated thus leading to enhanced packing within the powder. Overall, the bulk density measured for the mixtures prepared in the high-intensity mixer are in a similar range compared to those of the assisted fluidized bed with a nozzle diameter of a 0.4 mm and distance to the distributor plate of 1 cm. This further corrobates that similar microstructures were obtained with both mixing devices.

LIC comminution is the governing factor that leads to a decrease in the electronic powder conductivity due to its insulating nature. To further underline this effect, the conductivity was plotted against the median LIC particle size obtained from the SEM image analysis (Fig. 7). A strong decrease in the electronic powder conductivity with increasing tip speed (high-intensity mixer) or mixing time (assisted fluidized bed) can be seen. Simultaneously to LIC comminution also deagglomeration of CB occur, which amplifies this decreasing trend but cannot be sufficiently well quantified via SEM analysis. Notably, both the high-intensity mixer and the assisted fluidized bed follow the same trend, suggesting that both devices achieve a similar microstructural state. However, slightly higher electronic conductivities become evident for the assisted fluidized bed at same LIC particle sizes indicating a less significant CB deagglomeration. This might be due to the reagglomeration mechanisms that continuously occur within the assisted fluidized bed. Moreover, according to earlier investigations [37], CB agglomerates can be dispersed particularly well by high shear stresses acting in the gap between the rotor blades and the chamber wall, leading to stronger deagglomeration/deaggregation of the CB agglomerates and aggregates.

3.4. Electrochemical behavior of SBB mixtures

The microstructural changes, e.g. LIC comminution as well as CB deagglomeration, mainly results in changes in the number of heterocontacts between LIC-LFP-CB as well as CB based electronic pathways and thus influence the achievable specific discharge capacities. A decrease in LIC particle size should be beneficial for the discharge capacity as it increases the number of ionic percolation paths within the SSB mix and thus increases the utilization of LFP particles [14,26]. On the other hand, CB deagglomeration and LIC comminution lead to a decreased electronic conductivity which could lead to a decrease in the discharge capacity when less LFP particles are electronically connected.

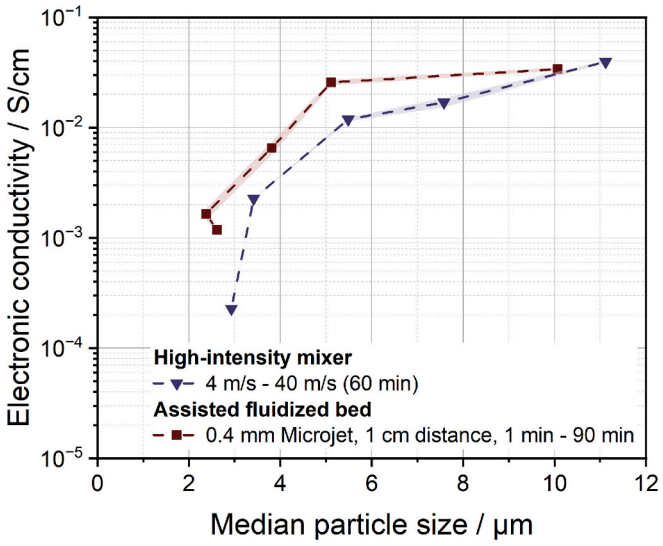


Fig. 7. Dependence of LIC particle size on the electronic powder conductivity of the SSB mixtures.

When examining the mean specific discharge capacity of mixtures produced in the assisted fluidized bed (0.4 mm nozzle diameter) and in the high-intensity mixer at 20 m/s and 40 m/s tip speed across different mixing times, a continuous increase in specific discharge capacity is observed (Fig. 8a). This indicates that a larger fraction of LFP particles is utilized during cyclization with an increase in mixing time, which results from the ongoing comminution of LIC particles. The reduction in LIC particle size and more homogeneous distribution hence enhances ionic percolation within the cathode, leading to higher accessible capacity. This relationship becomes particularly evident from the discharge capacity as a function of the median LIC particle size (Fig. 8b). Both the high-intensity mixer and the vibration fluidized bed exhibit an inverse correlation between discharge capacity and median LIC particle size: smaller particles yield higher capacities. This correlation originates from the improved ionic percolation within the SSB cathode at 0.1C mixture, which enhances the connectivity of the active material to the ionic network.

Although a strong decrease in electronic conductivity was detected, the discharge capacity nevertheless continues to rise. This suggests that, even after significant deagglomeration of CB and comminution of LIC, which reduces electronic contact points, the electronic percolation network is not the limiting factor at 0.1C in this material system. Instead, the dominant limiting factor is the homogeneous distribution of the LIC, LFP and CB particles within the composite and the solid electrolyte particle size, which must be minimized to maximize the achievable discharge capacity. The importance of the electronic percolation will probably increase at higher C-rates.

Comparing the high-intensity mixer discharge capacity progressions, a higher maximum terminal discharge capacity of about 110 mAh/g is reached at the higher rotational speed and thus stress intensity. This implies that the tip speed and thus stress intensity is the governing factor for LIC comminution and thus achievable discharge capacity. In comparison, the mixtures prepared with the assisted fluidized bed reached a

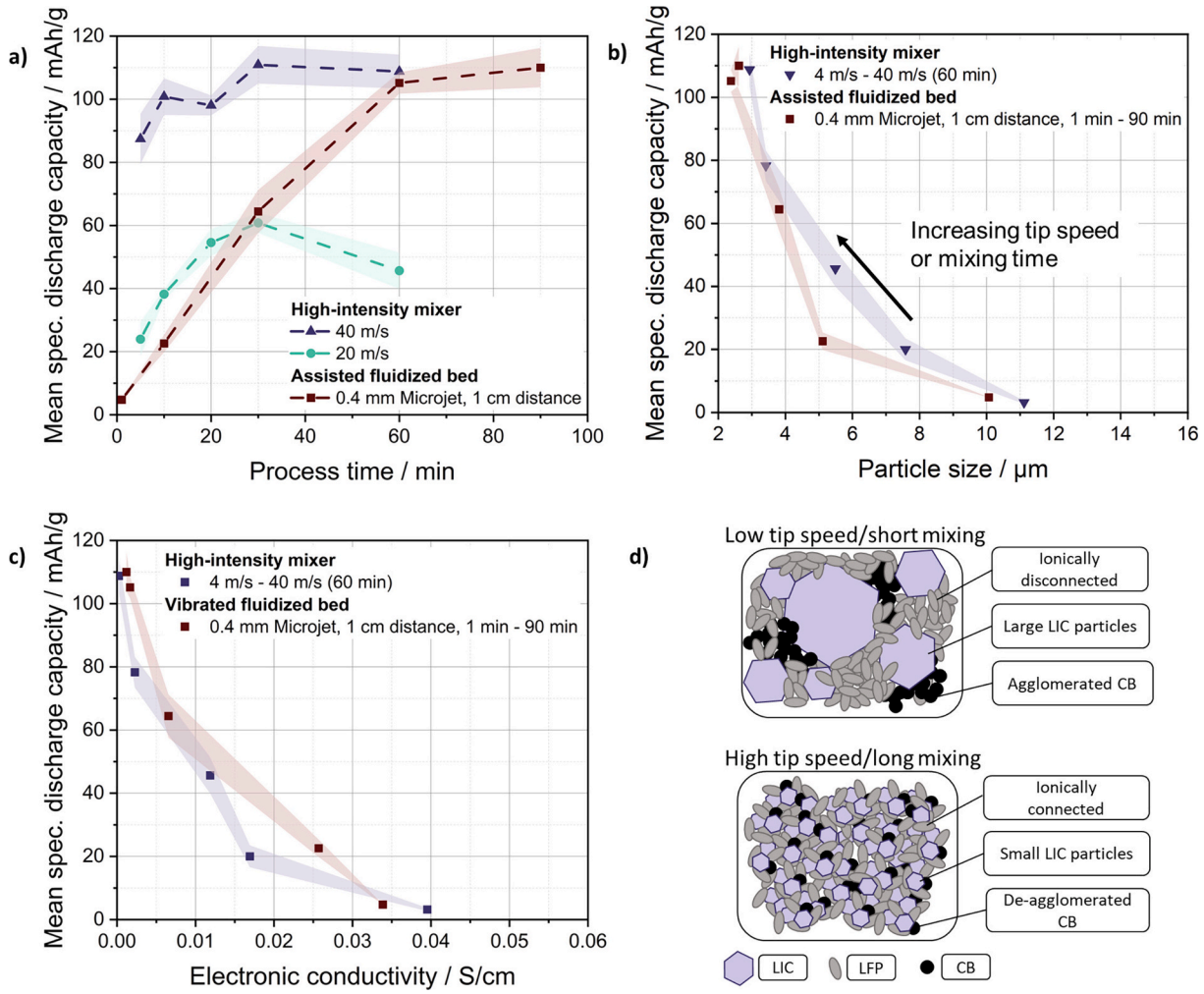


Fig. 8. a) Mean specific discharge capacity of 10 cycles at 0.1C for the SSB mixtures obtained from high-intensity mixing as well as assisted fluidized bed mixing at different mixing times. b) Mean specific discharge capacity as a function of the LIC median particle size obtained from SEM image analysis. c) Property-Property relationship between the electronic powder conductivity and the mean specific discharge capacity. d) Schematic representation of the main microstructural changes upon tip speed increase (high-intensity mixer) and mixing time increase (assisted fluidized bed).

comparable terminal capacity of also 110 mAh/g after 60 min of mixing. However, the comminution and deagglomeration rate of the process differ significantly: the high-intensity mixer reached this discharge capacity and thus microstructure after 30 min with 15 g of SSB cathode powder, whereas the assisted fluidized bed required 60 min for 100 g. This suggests that while both devices are effective in achieving the necessary microstructural state, the high-intensity mixer provides a higher specific frequency (frequency per mass of particles) of effective stressing events, accelerating the process.

The inability of the low-intensity mixing parameters (assisted fluidized bed: 0.8 mm nozzle, 10 cm distance; high-intensity mixer at 20 m/s) to achieve the terminal discharge capacity of 110 mAh/g indicates that stress intensity is below the needed fracture energy for LIC comminution [38,40]. The lower tip speeds, larger nozzle diameters, and greater processing distances did not exceed the breakage strength of the smaller LIC particles, thereby preventing the formation of a sufficient ionic percolation network regardless of mixing time.

Finally, it is important to note that with both processes the theoretical capacity of LFP (~150 mAh g^{-1}), is not reached for the SSB mixtures. This indicates that even at the highest applied stress intensities, the microstructure still exhibits limitations, and a significant fraction of the active material remains insufficiently connected to the ionic and/or electronic network and is kinetically hindered. This might be particle size related as smaller LIC particles could further increase the discharge capacity, or another limiting factor could be the composition of 58 wt% LFP, 38 wt% of LIC and 4 wt% of CB which could limit the theoretically highest number of possible heterocontacts.

Finally, measuring cell capacities, as done with a half-cell setup in this study, can be a time-consuming and costly process. As besides discharge capacity, also significant changes were observed for the electronic powder conductivity (cf. Fig. 6a,b), we plotted the discharge capacity as a function of the electronic conductivity (Fig. 8c). Here it becomes evident, that there is a strong correlation between the electronic conductivity and the discharge capacity in used material system. The lower the electronic conductivity, the higher the discharge capacity. In turn, at a given mixture composition, measurement of the electronic powder conductivity, which is considerably faster and simpler, could provide a reasonable indication of microstructural changes (LIC comminution and CB deagglomeration) and thereby serve as a proxy for the achievable discharge capacities in this material system.

In summary, both the assisted fluidized bed and the high-intensity mixer are capable of producing SSB mixtures with discharge capacities of up to approximately 110 mAh/g. These capacities increase as the LIC particle size decreases as schematically shown in Fig. 8d. The reachable LIC particle size, however, is limited by the stress intensity generated within each process. For better specific discharge capacities higher stress intensities as for example by high intensity ball mills have to be applied.

3.5. Influence of specific energy input

In order to evaluate the efficiency of the assisted fluidized bed and the high-intensity mixer, the specific energy input of both devices is compared. In the case of the high-intensity mixer, the electrical power was measured both with (overall power P) and without powder (no-load power P_0). The difference represents the net power that is used during processing. By integrating this power curve over time and dividing it by the total powder mass m the total specific energy input of the mixer $E_{m,M}$ is calculated.

$$E_{m,M} = \frac{E_{m,p}}{\nu} = \frac{\int (P - P_0)dt}{m} \tag{4}$$

However, this mixer related specific energy input is not the specific energy that is transferred to the product particles $E_{m,p}$. To express $E_{m,p}$, an additional energy transfer coefficient ν is necessary which takes into account the dissipation of energy through frictional losses [38].

For the assisted fluidized bed, electrical power is not a suitable indicator since the powder is processed primarily by gas flows. Energy contributions from fluidization gas and vibration are negligible compared to the high-velocity jet. Therefore, this study considers only the kinetic energy of the jet as well as the expansion of the gas (Eq. (5)) [49].

$$E_M = \dot{m} \bullet w_t = A \bullet p_o \sqrt{\frac{\kappa}{R_s \bullet T_o} \bullet \left(\frac{2}{\kappa + 1}\right)^{\frac{\kappa+1}{\kappa-1}}} \bullet c_p \bullet T_0 \left[1 - \left(\frac{p_1}{p_0}\right)^{\frac{\kappa-1}{\kappa}}\right] \tag{5}$$

Fig. 9 shows the mean specific discharge capacity as a function of the specific energy input for both the high-intensity mixer and the assisted fluidized bed. In general, the mean discharge capacity increased with increased specific energy input for both mixing devices. For the high-intensity mixer at tip speeds of 20 m/s and 30 min of mixing, discharge capacities of 60 mAh/g with a specific energy input of roughly 1000 kJ/kg are reached. By increasing the tip speed to 40 m/s the specific energy input increases to a range of 4000–6000 kJ/kg, resulting in the highest observed capacity of 110 mAh/g. To reach similar specific discharge capacities with the assisted fluidized bed approximately 1000 kJ/kg are required for the 0.4 mm jet with 1 cm nozzle. This reveals, that for the given set-up, the assisted fluidized bed seems to need approximately 4 to 6 times less specific energy to create a comparable microstructure to the high-intensity mixer. One possible explanation for this is that specific energy introduced via the gas jet is transferred more efficiently, resulting in a higher ratio of effective to non-effective stressing events within the assisted fluidized bed. In contrast, the high-intensity mixer appears to exhibit a much lower energy transfer coefficient, with a significant fraction of the mixer-related specific energy input dissipated through frictional losses [38].

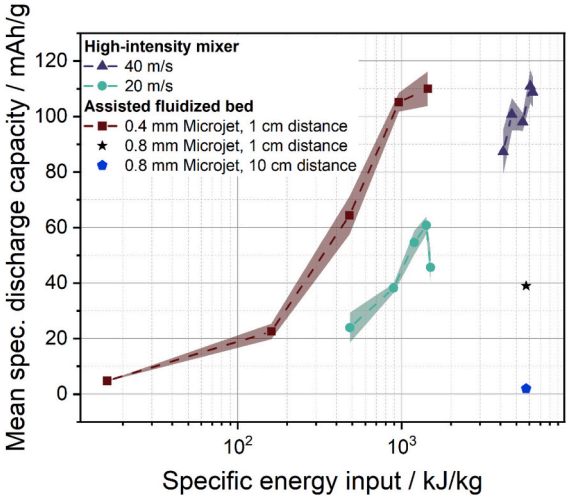


Fig. 9. Mean specific discharge capacity as a function of the specific energy input by the high-intensity mixer and assisted fluidized bed.

The comparatively poor utilization of the overall number of stressing events due to the low ratio of effective to non-effective stressing events in the high-intensity mixer may be attributed to frictional losses and material adhesion to the mixer walls after short mixing times. As a result, only a limited fraction of the material is effectively subjected to stressing, reducing the overall process efficiency.

For the assisted fluidized bed with a larger nozzle (0.8 mm), the specific energy input is approximately four times higher than that of the 0.4 mm nozzle due to the increased gas mass flow. Despite this, the 0.8 mm nozzle configuration proved insufficient to achieve the threshold stress intensity required for effective particle processing, despite the higher total energy input. Furthermore, by increasing the nozzle distance from 1 to 10 cm (while keeping the nozzle diameter at 0.8 mm) did not lead to a significant activation of LFP with the same specific energy input from the jet. This suggests, that besides stress intensity, the number of stressing events and the ratio of effective to non-effective stressing events is crucial to comminute LIC and to create a well performing SSB microstructure.

Overall, the observed efficiency difference between the high-intensity mixer and the assisted fluidized bed highlights their different stressing mechanisms: the high-intensity mixer transfers energy via direct mechanical impact to almost the entire mass in the process, where a large portion is dissipated due to frictional losses. In contrast, the assisted fluidized bed concentrates energy in a small, high-impact zone in which only a small part of the overall material mass is stressed at once, possibly leading to an increased ratio of effective stressing events. However, although the fluidized bed appears to be more efficient in terms of specific energy input, the overall system efficiency is significantly reduced by the compressor's energy demand, which was not considered in this study.

3.6. Remarks on scalability

While both processes yield comparable microstructures and electrochemical performances, their scaling logic differs fundamentally due to the underlying stressing mechanisms. The development of the SSB microstructures is primarily governed by the stress intensity and ratio of effective to non-effective stressing events. For a scale-up the specific number of sufficient stress events, i.e. stress events with sufficient stress intensity is decisive and should scale at least linearly with process size.

The stress intensity in the high-intensity mixer is primarily governed by the shear and impact stress and thus, by the rotor tip speed at constant gap width. For a successful scale-up, it is essential to maintain a constant tip speed while preserving a narrow gap between the rotor and the mixing chamber wall, ensuring frequent particle-rotor collisions and effective shear forces required for deagglomeration. Scale-up can be achieved by increasing the mixer diameter and length by keeping the gap width ideally constant.

For the scale-up of the assisted fluidized bed, keeping the stress intensity constant could be achieved by keeping the flow regime similar: keeping the number of jets to area ratio as well as the superficial gas velocity constant. At the same time, the gas velocity must be carefully minimized to limit particle losses due to elutriation. In contrast to the high-intensity mixer, where heat dissipation through friction poses a major challenge, if the gap width is increased, the assisted fluidized bed remains thermally stable. As elutriation cannot be completely avoided, efficient particle recovery systems, such as filtration units and mechanical vibration, are essential to reduce material losses in large-scale production.

3.7. Conclusion

The assisted fluidized bed as well as the high-intensity mixer were shown to be suitable for the dry mixing of fine particles for SSB cathode composites. Besides mixing, also comminution and deagglomeration mechanisms take place, which are crucial for an improvement in the achievable discharge capacity. For the applied model material system consisting of LFP, LIC and CB, discharge capacities ranging from <5 mAh/g up to 110 mAh/g could be reached, depending on the process parameters applied. This significant variation in achievable discharge capacity mainly stems from the reduction in solid electrolyte particle size, leading to a more homogeneous microstructure with increased number of electrochemically addressed LFP particles. During processing, the stress intensity is the primary factor for comminution and deagglomeration, which means that it also determines the SSB microstructure. Low-stress intensities fail to sufficiently comminute LIC particles, leading to poor cell performance.

An inverse correlation is observed between the electronic powder conductivity and the resulting cell capacity. The mixing process disrupts long-range electronic percolation pathways due to the pronounced deagglomeration of CB and the comminution of insulating LIC. At the same time, the reduction of LIC particle size enhances long-range ionic percolation, which in turn significantly improves the cell capacity. A strong correlation between electronic powder conductivity and the achieved discharge capacity at 0.1C was observed, indicating that the much simpler and faster powder-conductivity measurement can serve as an initial indicator of the resulting microstructure and thus of the effectiveness of the mixing process for this material system. While the powder conductivity measurements suggest a disruption of the long-range electronic percolation network, we acknowledge that this is an indirect measurement performed on compacted pellets. Future studies employing direct visualization techniques, such as 3D FIB-SEM tomography, are essential to validate proposed microstructural mechanisms. Transferring the parameters identified in this study to other material systems will require specific calibrations of the processing stress intensities, depending on the material system. This requires deep experimental studies on the mixing behavior with sulfide and oxide SEs.

As for the stressing events, the high-intensity mixer relies on rotor tip speed to generate stress events with high intensities, while the assisted fluidized bed relies on particle-wall collisions caused by high particle velocities of higher gas pressures. Both methods offer different upscaling strategies: The high-intensity mixer can be upscaled by increasing the mixer size, if the tip speed and shear gap width is maintained. The assisted fluidized bed is scalable via reactor diameter and nozzle count, but it strictly requires maintaining a low superficial gas velocity to reduce particle deceleration, small nozzle geometry and height, and implementing sophisticated filtering strategies to prevent particle elutriation.

Overall, we were able to show that both mixing devices are suitable and scalable for mixing of SSB cathode mixtures with very fine particles. Furthermore, the discharge capacity increased with increasing energy input. However, it should be noted that the LIC–LFP–CB system represents a model battery system, and future studies should therefore focus on more industrially relevant compositions, particularly those on NMC-based active materials and sulfide solid electrolytes [15], to further demonstrate the applicability of both mixing technologies for practical large-scale processing. Further studies should include binder integration and optimized cell design to study the degradation during long-term cycling.

Declaration of generative AI and AI-assisted technologies in the manuscript preparation process

During the preparation of this work, the author(s) used image generation tools (specifically ChatGPT/DALL-E 3, Gemini, and Microsoft Copilot) to assist in rendering new device images based on original sketches. After generating these images, the authors reviewed, validated, and edited the visual content for technical accuracy as needed, and take full responsibility for the content of the published article.

CRediT authorship contribution statement

Zhi Cheng Hua: Writing – review & editing, Writing – original draft, Visualization, Validation, Resources, Methodology, Investigation, Formal analysis, Data curation, Conceptualization. **Finn Frankenberg:** Writing – review & editing, Writing – original draft, Visualization, Validation, Resources, Methodology, Investigation, Formal analysis, Data curation, Conceptualization. **Maximilian Kissel:** Writing – review & editing, Visualization, Methodology, Investigation, Data curation, Conceptualization. **Jürgen Janek:** Writing – review & editing, Supervision, Funding acquisition. **Stefan Heinrich:** Writing – review & editing, Supervision, Funding acquisition. **Arno Kwade:** Writing – review & editing, Supervision, Funding acquisition.

Declaration of competing interest

The authors declare that they have no known competing financial interests or personal relationships that could have appeared to influence the work reported in this paper.

Acknowledgements

This research was funded by the Deutsche Forschungsgemeinschaft (DFG, German Research Foundation) – project no. 462470125 (F. Frankenberg, A. Kwade, M. Kissel, J. Janek) and 462397288 (Z. Hua, S. Heinrich).

Appendix A. Supplementary data

Supplementary data to this article can be found online at https://doi.org/10.1016/j.powtec.2026.123155.

Data availability

Data will be made available on request.

References

[1] J. Janek, W.G. Zeier, Nat. Energy (2016), https://doi.org/10.1038/nenergy.2016.141.
[2] J. Mun, T. Song, M.-S. Park, J.H. Kim, Adv. Mater. (2025), https://doi.org/10.1002/adma.202506123 e2506123.
[3] M. Gao, H. Li, L. Xu, Q. Xue, X. Wang, Y. Bai, C. Wu, J. Energy Chem. 59 (2021) 666–687, https://doi.org/10.1016/j.jechem.2020.11.034.
[4] J. Janek, W.G. Zeier, Nat. Energy 8 (3) (2023) 230–240, https://doi.org/10.1038/s41560-023-01208-9.
[5] P. Lu, S. Gong, C. Wang, Z. Yu, Y. Huang, T. Ma, J. Lian, Z. Jiang, L. Chen, H. Li, F. Wu, ACS Nano 18 (10) (2024) 7334–7345, https://doi.org/10.1021/acsnano.3c07023.
[6] W. Zaman, Le Zhao, T. Martin, X. Zhang, Z. Wang, Q.J. Wang, S. Harris, K. B. Hatzell, ACS Appl. Mater. Interfaces 15 (31) (2023) 37401–37409, https://doi.org/10.1021/acsami.3c05886.
[7] Y. Wu, J. Xu, P. Lu, J. Lu, L. Gan, S. Wang, R. Xiao, H. Li, L. Chen, F. Wu, Adv. Energy Mater. (2023), https://doi.org/10.1002/aenm.202301336.
[8] F. Hippauf, B. Schumm, S. Doerfler, H. Althues, S. Fujiki, T. Shiratsuchi, T. Tsujimura, Y. Aihara, S. Kaskel, Energy Storage Mater. 21 (2019) 390–398, https://doi.org/10.1016/j.ensm.2019.05.033.
[9] J. Hong, J. Yoon, J.-W. Park, Y.-C. Ha, J. Lee, I. Hwang, J. Power Sources 655 (2025) 237925, https://doi.org/10.1016/j.jpowsour.2025.237925.
[10] D. Lee, Y. Shim, Y. Kim, G. Kwon, S.H. Choi, K. Kim, D.-J. Yoo, Nat. Commun. 15 (1) (2024) 4763, https://doi.org/10.1038/s41467-024-49183-3.
[11] N. Kühn, F. Frankenberg, A. Kwade, C. Schilde, J. Colloid Interface Sci. 680 (Pt A) (2025) 696–713, https://doi.org/10.1016/j.jcis.2024.10.187.
[12] J. Witte, Z.C. Hua, V. Kolck, H. Kruggel-Emden, S. Heinrich, E. Schmidt, Processes 11 (11) (2023) 3243, https://doi.org/10.3390/pr11113243.
[13] J. Witte, V. Kolck, H. Kruggel-Emden, E. Schmidt, Chem. Ing. Tech. (2026), https://doi.org/10.1002/cite.70039.

[14] M. Kissel, M. Schosland, J. Töws, D. Kalita, Y. Schneider, J. Kessler-Kühn, S. Schröder, J. Schubert, F. Frankenberg, A. Kwade, A. Bielefeld, F.H. Richter, J. Janek, Adv. Energy Mater. (2025), https://doi.org/10.1002/aenm.202405405.
[15] F. Frankenberg, C.A. Heck, M. Kissel, M.A. Lange, V. Faka, A. Diener, P. Haase, P. Michalowski, W.G. Zeier, J. Janek, A. Kwade, Small (Weinheim an der Bergstrasse, Germany) 21 (41) (2025) e07279, https://doi.org/10.1002/smll.202507279.
[16] E. Schlautmann, A. Weiß, O. Maus, L. Ketter, M. Rana, S. Puls, V. Nickel, C. Gabbey, C. Hartnig, A. Bielefeld, W.G. Zeier, Adv. Energy Mater. (2023), https://doi.org/10.1002/aenm.202302309.
[17] R. Guo, K. Zhang, W. Zhao, Z. Hu, S. Li, Y. Zhong, R. Yang, X. Wang, J. Wang, C. Wu, Y. Bai, Energy Mater. Adv. (2023), https://doi.org/10.34133/energymatadv.0022.
[18] P. Minnmann, J. Schubert, S. Kremer, R. Rekers, S. Burkhardt, R. Ruess, A. Bielefeld, F.H. Richter, J. Janek, J. Electrochem. Soc. 171 (6) (2024) 60514, https://doi.org/10.1149/1945-7111/ad510e.
[19] P. Minnmann, F. Strauss, A. Bielefeld, R. Ruess, P. Adelhelm, S. Burkhardt, S. L. Dreyer, E. Trevisanello, H. Ehrenberg, T. Brezesinski, F.H. Richter, J. Janek, Adv. Energy Mater. (2022), https://doi.org/10.1002/aenm.202201425.
[20] S. Noh, W.T. Nichols, M. Cho, D. Shin, J. Electroceram. 40 (4) (2018) 293–299, https://doi.org/10.1007/s10832-018-0129-y.
[21] A. Kwade, W. Haselrieder, R. Leithoff, A. Modlinger, F. Dietrich, K. Droeder, Nat. Energy 3 (4) (2018) 290–300, https://doi.org/10.1038/s41560-018-0130-3.
[22] O. Maus, M.A. Lange, F. Frankenberg, F. Stainer, V. Faka, E. Schlautmann, C. Rosenbach, A. Jodlbauer, J. Schubert, J. Janek, C. Li, P. Michalowski, H.M. R. Wilkening, A. Kwade, W.G. Zeier, Adv. Energy Mater. (2025), https://doi.org/10.1002/aenm.202403291.
[23] R. Rajagopal, Y. Subramanian, K.-S. Ryu, RSC Adv. 11 (52) (2021) 32981–32987, https://doi.org/10.1039/d1ra05897e.
[24] A. Bielefeld, D.A. Weber, J. Janek, J. Phys. Chem. C 123 (3) (2019) 1626–1634, https://doi.org/10.1021/acs.jpcc.8b11043.
[25] Z.C. Hua, F. Frankenberg, M. Kissel, J. Janek, A. Kwade, S. Heinrich, Powder Technol. 458 (2025) 120906, https://doi.org/10.1016/j.powtec.2025.120906.
[26] F. Frankenberg, M. Kissel, C.F. Burmeister, M. Lippke, J. Janek, A. Kwade, Powder Technol. 435 (2024) 119403, https://doi.org/10.1016/j.powtec.2024.119403.
[27] L. Fernandez-Diaz, J. Castillo, E. Sasieta-Barrutia, M. Arnaiz, M. Cabello, X. Judez, A. Terry, L. Otaegui, M.C. Morant-Miñana, A. Villaverde, Chem. Eng. J. 464 (2023) 142469, https://doi.org/10.1016/j.cej.2023.142469.
[28] L. Peng, C. Yu, Z. Zhang, R. Xu, M. Sun, L. Zhang, S. Cheng, J. Xie, Energy Environ. Mater. (2023), https://doi.org/10.1002/eem2.12308.
[29] L.F. Hakim, J.L. Portman, M.D. Casper, A.W. Weimer, Powder Technol. 160 (3) (2005) 149–160, https://doi.org/10.1016/j.powtec.2005.08.019.
[30] J.A. Quevedo, A. Omosebi, R. Pfeffer, AICHE J. 56 (6) (2010) 1456–1468, https://doi.org/10.1002/aic.12075.
[31] T.-T. Lv, J. Liu, L.-J. He, H. Yuan, T.-Q. Yuan, J. Energy Chem. 98 (2024) 414–421, https://doi.org/10.1016/j.jechem.2024.07.003.
[32] M. Alonso, F.J. Alguacil, Rev. Metal. 35 (5) (1999) 315–328, https://doi.org/10.3989/revmetalm.1999.v35.i5.640.
[33] L.T. Fan, Y. Chen, F.S. Lai, Powder Technol. 61 (3) (1990) 255–287, https://doi.org/10.1016/0032-5910(90)80092-D.
[34] M. Kissel, F. Frankenberg, T. Demuth, A. Lai, N. Laser, D. Wagner, A. Eisa, P. Michalowski, K. Volz, A. Kwade, J. Janek, Nat. Commun. (2026), https://doi.org/10.1038/s41467-026-71305-2.
[35] Proceedings of the 58th Conference on Simulation and Modelling (SIMS 58) Reykjavik, Iceland, September 25th – 27th, 2017, Linköping Electronic Conference Proceedings, Linköping University Electronic Press, 2017.
[36] A. Bielefeld, D.A. Weber, R. Rueß, V. Glavas, J. Janek, J. Electrochem. Soc. 169 (2) (2022) 20539, https://doi.org/10.1149/1945-7111/ac50df.
[37] H. Bockholt, W. Haselrieder, A. Kwade, Powder Technol. 297 (2016) 266–274, https://doi.org/10.1016/j.powtec.2016.04.011.
[38] A. Kwade, Chem. Eng. Technol. 26 (2) (2003) 199–205, https://doi.org/10.1002/ceat.200390029.
[39] B. Koeninger, T. Hensler, S. Romeis, W. Peukert, K.-E. Wirth, Powder Technol. 327 (2018) 346–357, https://doi.org/10.1016/j.powtec.2017.12.084.
[40] A. Kwade, Powder Technol. 105 (1–3) (1999) 382–388, https://doi.org/10.1016/S0032-5910(99)00162-X.
[41] A. Sakuda, A. Hayashi, Y. Takigawa, K. Higashi, M. Tatsumisago, J. Ceram. Soc. Jpn. 121 (1419) (2013) 946–949, https://doi.org/10.2109/jcersj2.121.946.
[42] A. Sakuda, A. Hayashi, M. Tatsumisago, Sci. Rep. 3 (2013) 2261, https://doi.org/10.1038/srep02261.
[43] H. Kim, K. Hikima, K. Watanabe, N. Matsui, K. Suzuki, S. Obokata, H. Muto, A. Matsuda, R. Kanno, M. Hirayama, Mater. Trans. 65 (8) (2024) 861–866, https://doi.org/10.2320/matertrans.MT-Y2024001.
[44] M. Papakyriakou, M. Lu, Y. Liu, Z. Liu, H. Chen, M.T. McDowell, S. Xia, J. Power Sources 516 (2021) 230672, https://doi.org/10.1016/j.jpowsour.2021.230672.
[45] K. Kim, D. Park, H.-G. Jung, K.Y. Chung, J.H. Shim, B.C. Wood, S. Yu, Chem. Mater. 33 (10) (2021) 3669–3677, https://doi.org/10.1021/acs.chemmater.1c00555.
[46] X. Li, J. Liang, N. Chen, J. Luo, K.R. Adair, C. Wang, M.N. Banis, T.-K. Sham, L. Zhang, S. Zhao, S. Lu, H. Huang, R. Li, X. Sun, Angew. Chem. 131 (46) (2019) 16579–16584, https://doi.org/10.1002/ange.201909805.
[47] H.C.H. Rumpf, Chem. Ing. Tech. 42 (8) (1970) 538–540, https://doi.org/10.1002/cite.330420806.
[48] L. Tavares, R. King, Int. J. Miner. Process. 54 (1) (1998) 1–28, https://doi.org/10.1016/S0301-7516(98)00005-2.
[49] H.D. Baehr, S. Kabelac, Thermodynamik, Springer Berlin Heidelberg, Berlin, Heidelberg, 2016.